Elucidating the Role of Prelithiation in Si-based Anodes for Interface Stabilization

Shuang Bai, Wurigumula Bao, Kun Qian, Bing Han, Weikang Li, Baharak Sayahpour, Bhagath Sreenarayanan, Darren H.S. Tan, So-yeon Ham, and Ying Shirley Meng*

Prelithiation as a facile and effective method to compensate the lithium inventory loss in the initial cycle has progressed considerably both on anode and cathode sides. However, much less research has been devoted to the prelithiation effect on the interface stabilization for long-term cycling of Si-based anodes. An in-depth quantitative analysis of the interface that forms during the prelithiation of SiO_x is presented here and the results are compared with prelithiaton of Si anodes. Local structure probe combined with detailed electrochemical analysis reveals that a characteristic mosaic interface is formed on both prelithiated SiO_x and Si anodes. This mosaic interface containing multiple lithium silicates phases, is fundamentally different from the solid electrolyte interface (SEI) formed without prelithiation. The ideal conductivity and mechanical properties of lithium silicates enable improved cycling stability of both prelithiated anodes. With a higher ratio of lithium silicates due to the oxygen participation, prelithiated $SiO_{1.3}$ anode improves the initial coulombic efficiency to 94% in full cell and delivers good cycling retention (77%) after 200 cycles. The insights provided in this work can be used to further optimize high Si loading (>70% by weight) based anodes in future high energy density batteries.

1. Introduction

The success of lithium-ion batteries (LIBs) stems from the rapidly growing efforts in battery research and development, leading to vast improvements in materials performance and decrease in production costs. The justification for a more widespread adoption of LIBs entails overcoming fundamental obstacles such as demands for higher energy and power density, cycle life, less safety hazards and lowered costs of batteries per kWh. For instance, LIBs need to achieve energy densities of more than 350 Wh kg^{-1} to better meet market demands.[1] Compared to the cathode development, which has seen extensive improvements in both reversible capacity and nominal cell voltage,[2] the anode has not experienced as much progress from traditional graphite-based anodes used in today's LIBs. Si-based anodes exhibit high theoretical specific capacities (3580 mAh g^{-1} for Si and >2000 mAh g^{-1} for SiO_x depending on x value) and potential close to Li metal (0.3 V *vs.* Li/Li$^+$),[3,4] making it capable of realizing high energy density in LIBs. Moreover, its relative elemental abundance and environmental friendliness make it both cost effective and sustainable for large scale adoption in LIBs.

Despite the high theoretical energy density of Si (Figure S1, Supporting Information), the poor cycling performance resulting from the continuous interfacial growth and Li inventory consumption leads to poor active material utilization in the commercial level applications.[5] Together with the high cost of mass production, the commercialization of nanosized silicon as an anode material for lithium-ion batteries has been largely impeded. SiO_x emerging as an alternative affordable, high energy density anode draws great interest for the good cycling stability and active material utilization. However, the initial coulombic efficiency (ICE) of silicon-based anodes is relatively low, which is associated with the electrolyte decomposition, formation of solid electrolyte interface (SEI), irreversible parasitic reactions (such as Li_2O and lithium silicates formation for SiO_x).[6]

Even though strategies like innovated electrolytes have been reported, lithium loss in the initial cycle of Si-based materials is way higher than that of the commercial graphite.[7–9] This higher

S. Bai, B. Sayahpour, S.-yeon Ham, Y. S. Meng
Materials Science and Engineering
University of California San Diego
La Jolla, CA 92093, United States
E-mail: shirleymeng@uchicago.edu
W. Bao, Y. S. Meng
Pritzker School of Molecular Engineering
University of Chicago
Chicago, IL 60637, United States
K. Qian, B. Han, W. Li, B. Sreenarayanan, D. H. Tan, Y. S. Meng
Department of NanoEngineering
University of California San Diego
La Jolla, CA 92093, United States

active lithium loss is detrimental to the specific energy density of the full cell consisting of a silicon-based anode and a positive electrode with limited lithium amount. Therefore, a promising approach, prelithiation, by presetting lithium ions in the anode material before electrochemical cycling is effective in compensating for the initial Li loss, resulting in improved energy density of full cells.[10] Based on the different protocols and mechanisms, the prelithiation strategies on the Si-based anodes can be divided into two categories: electrochemical method and chemical method.[11] The chemical method, including mechanical alloy and one-pot metallurgy by mixing anode materials (e.g., Si,[12] SiO_x[13]) and Li source, is scalable to prepare lithiated anode materials. However, it is difficult to accurately control the degree of prelithiation with the chemical method and prepare electrodes on a large scale due to the sensitivity of the lithiated anode materials to the environment. The electrochemical method by architecting half-cell structure composed of Si-based electrodes and Li metal foil is widely used in lab scale, in which the prelithiation amount can be controlled by the voltage or the prelithiation time.[14,15] To avoid complex operations caused by half-cell electrochemical method, an advanced strategy was proposed to contact the Si-based anode directly with Li metal foil and electrolyte in between.[16] The direct contact method creates short-circuit, and the electrons will move immediately at the point of contact under the action of the electric field. To remain electrically neutral, the Li metal will release lithium ions through the electrolyte into the anode material to complete the lithiation process. This short-circuit electrochemical method utilizing the self-discharge of lithium metal can be processed in a simple assembly and the prelithiation time can reflect the pre-lithiation degree mediately.

Although there is no doubt that the prelithiation of Si-based anodes can improve the ICE, as shown in Table S1 (Supporting Information),[16–26] the impact of prelithiation on long-term cycling stability in the full cell remains elusive. Kim et al. reported the capacity retention of the prelithiated SiO_x/NCA (Li[$Ni_{0.8}Co_{0.15}Al_{0.05}$]$O_2$) full cell was 15% lower than the pristine counterpart after 100 cycles.[16] By using the prelithiated SiO_x, Chung et al. enhanced the energy density of full cell by 50% compared to that adopting pristine SiO_x with similar cycling retention (70% for the prelithiated anode *vs.* 75% for the pristine anode) over 800 cycles.[22] While cycling stability of full cells using prelithiated anodes were improved in other works,[17,19–21] the improvement was generally ascribed to the stable SEI layer established during the prelithiation process. Shen et al. applied X-ray photoelectron spectroscopy (XPS) to pinpoint the prelithiation products and it has been found that the SEI mainly contains Li_2CO_3 and LiF,[27] which has little difference compared to the components of SEI formed in the electrochemical reaction. The controversial results on the cycling stability by using the prelithiated Si-based anodes reflects the significant complexity of prelithiation process and challenges in characterization of the prelithiated products.

In this work, we systematically investigate the SEI components, structure, and properties for the prelithiation process in two representative Si-based anode materials, micro silicon (µSi) and silicon monoxide (SiO_x), to reveal insights into the prelithiation effects on the cycling stability of full cells with $LiFePO_4$ (LFP) cathode materials. Micron sized Si and SiO_x are selected in this study due to their cost effectiveness. The short-circuit elec-

trochemical method is applied in this study with high pressure ($\approx$5.5 kPa) onto Li metal foil and Si-based anodes to enable sufficient contact. After electrochemical analysis and X-ray diffraction (XRD) to characterize the prelithiated materials, we apply ex situ transmission electron microscopy (TEM) under cryogenic temperature to identify crystalline SEI components and their spatial distribution. In addition, XPS depth profiling is used to semi-quantitatively analyze the SEI composition for both crystalline and amorphous phases. We then compare the SEI composition and structure obtained from the prelithiation and electrochemical process, to investigate the physical properties of SEI and their impact on the interface stabilization over the cycling. The analysis reveals that the prelithiated interface comprises lithium silicates, lithium oxide, and byproducts of electrolyte decomposition. These components are uniformly blended within the interface, resulting in the formation of a mosaic microstructure. Owing to its high ratio of ionic-to-electronic conductivity ($\approx$10^3) and mechanical strength (Young's modulus of $\approx$120 GPa), the lithium silicates enriched SEI, which forms during the prelithiation process, imparts excellent long-term cycling stability.

2. Result and Discussion

2.1. ICE Improvement of Si-based Anode Materials by Prelithiation

To realize high volumetric energy density, micro sized Si and SiO_x are applied in the anode fabrication with high active material ratios (70% by weight). Unlike the diamond cubic crystal structure of µSi, the powder XRD pattern of SiO_x (Figure S2, Supporting Information) contains no sharp Bragg reflections and only diffuse scattering from the amorphous components are visible. To investigate the microstructure of pristine SiO_x, electron energy loss spectroscopy (EELS) was used, and the results are shown in Figure S3 (Supporting Information). The EELS spectra of the Si L-edge from the surface and bulk region of the particle, as indicated in high angle annular dark field (HAADF) images in Figure S3 (Supporting Information), is compared with the spectra acquired from the standard samples of Si and SiO_2. The comparison clearly indicates SiO_x contains two separate phases, Si and SiO_2. The Si local environment is similar between the bulk and surface region. These results are consistent with the proposed microstructure model, in which SiO_x consists of Si and SiO_2 including the sub-oxide interphase boundary layer making up 20%–25% of the total number of atoms.[28]

The oxygen content in SiO_x has a critical impact on structural changes that occur during electrochemical cycling.[29] The atomic ratio between O and Si is determined to be 1.32(2) by inductively coupled plasma mass spectrometry (ICP-MS) following the similar protocol as reported.[30] Prelithiated Si and $SiO_{1.3}$ anodes were then prepared by the short-circuit electrochemical method using the setup provided in Figure S4 (Supporting Information). Note external pressure is necessary to deal with the nonuniform prelithiation issues due to the uneven contact between silicon-based anodes and lithium metal. Pristine and prelithiated $SiO_{1.3}$ and µSi electrodes with different prelithiation time were then galvanostatically discharged to 50 mV and then charged to 1.5 V in half cell with Li metal as the counter electrode. As shown in **Figure 1**A,B, the charge (delithiation) capacity of prelithiated electrodes is
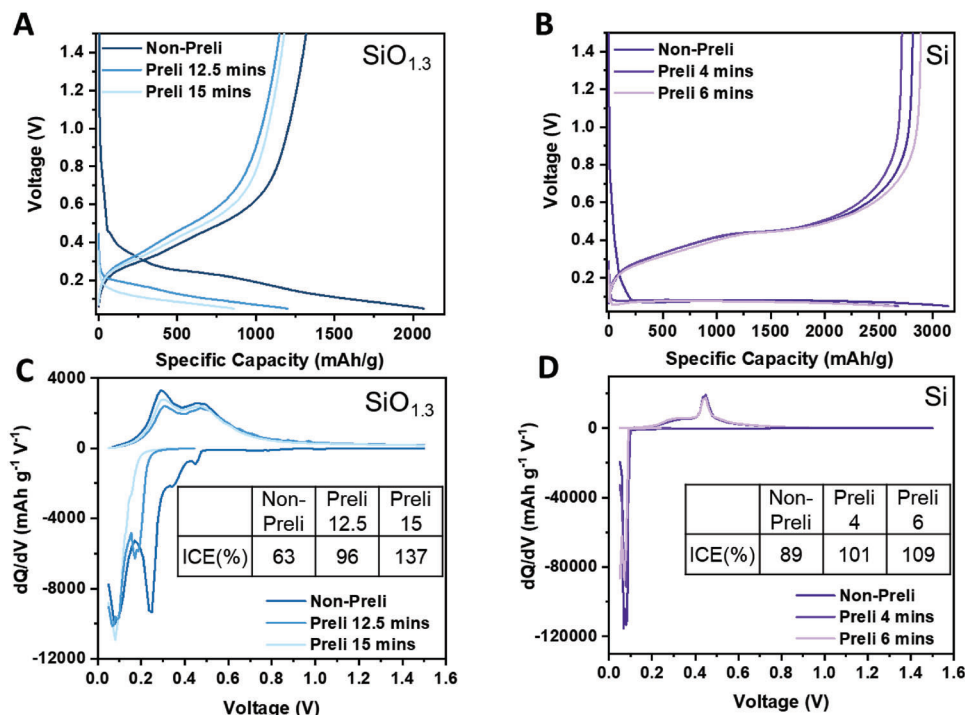
Figure 1. Voltage profile of $SiO_{1.3}$ A) for the first cycle and C) corresponding dQ/dV analysis in half cell with and without prelithiation. Voltage profile of μSi B) for the first cycle and D) corresponding dQ/dV analysis in half cell with and without prelithiation. The galvanostatic discharge/charge test in half cell was carried out at C/20-rate (1 C =2000 mAh g^{-1} for $SiO_{1.3}$ and 1 C=3400 mAh g^{-1} for μSi) for the initial cycle.

similar to the pristine electrode while the discharge (lithiation) capacity of prelithiated electrodes is lower than the pristine electrode. This indicates the insertion of lithium during the prelithiation process compensates for the lithium loss derived from the formation of irreversible byproducts, but hardly affect the reversible capacity. The optimized prelithiation time is 12.5 min for $SiO_{1.3}$ when the ICE reaches 96%, while shorter time (4 min) is required for Si to achieve the optimized ICE (101%). This difference is due to the thinner mass loading of Si anode to keep the same negative to positive electrode capacity ratio (N/P ratio) of 1.1–1.2 in the full cell setup.

The differential capacity curves for the non-prelithiated $SiO_{1.3}$ in Figure 1C display three distinctive peaks at above 0.3 (vs. Li/Li$^+$), 0.24 and ≈0.1 V upon discharging. The irreversible peaks above 0.3 V are related to the electrolyte decomposition process with the formation of byproducts (Li_2CO_3 and LiF), which is consistent with the previous results.[31,32] The second peak could correspond to the formation of lithium silicates and lithium oxide.[31] Upon further discharge of $SiO_{1.3}$ to ≈0.1 V, the redox reaction could be assigned to Li-Si alloy phase formation. This redox potential is like that seen for μSi when the discharge voltage reaches 0.1 V, suggesting similar Li_xSi reactions occur. Only the redox reactions at 0.24 and 0.1 V are partially reversible during the charge process with potential shifts to 300 and 450 mV, respectively. The irreversible reaction peaks disappear and the peaks below 0.3 V decrease for the prelithiated $SiO_{1.3}$, which indicates the prelithiation products contain both irreversible and reversible phases. The XRD pattern for the prelithiated $SiO_{1.3}$ (Figure S2, Supporting Information) contains Bragg reflections from $Li_{13}Si_4$, Li_4SiO_4, Li_2SiO_3, and Li_2O phases, which is con-

sistent with the differential capacity analysis. The electrochemical reactions of the μSi electrode are characterized by redox reactions observed at 0.1 V for the discharge and at 0.45 V in the subsequent charge process (Figure 1D). The presence of these clear voltage processes indicates that these reactions essentially proceed via two-phase reactions, whereas the reversible reactions correspond to the conversion between the crystalline Si structure and the amorphous Li_xSi or crystalline $Li_{15}Si_4$ phase. The prelithiation process of μSi mainly reduces the capacity from the Li-Si alloy reaction during the discharge.

The improvement of ICE from this work is then compared with other published results, as shown in **Figure 2**. For a fair comparison, all data are from half cells tested with a similar voltage range and C-rate. Data are available in Table S1 (Supporting Information). Our work not only demonstrates the highest active material ratio for both prelithiated μSi and SiO_x anodes, but also delivers the ideal ICE (close to 100%) that is critical for the full cell cycling stability evaluation. The inconsistent full cell cycling stability improvement by using prelithiated Si-based anodes in the published results may be ascribed to the lower ICE (Figure 2) and indelicate control of the prelithiation degree.

2.2. Improvement of Full Cell Cycling Stability by Prelithiated Si-based Anodes

The prelithiation effect on the long-term cycling does not manifest in the half cell testing (Figure S5, Supporting Information), owing to the presence of an unrestricted lithium reservoir originating from the Li metal anode. The prelithiated $SiO_{1.3}$ and μSi
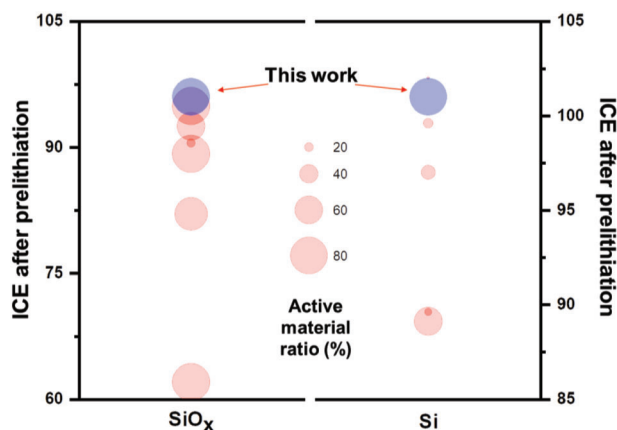
Figure 2. Literature summary on the ICE in half cell of prelithiated SiO_x and Si.[16–26]

were then paired with the LFP cathode to study the prelithiation effect on the long-term cycling stability of full cells. Olivine-type LFP was picked as the cathode active material in the full cell testing due to the structural stability. As shown in Figure S6 (Supporting Information), the LFP cathode with active material loading ≈1 mAh cm^{-2} can deliver 91% capacity retention after 200 cycles in half cell. The full cell cycling performance degradation can thus be reasonably correlated with the changes from Si-based anode side. The full cells using prelithiated $SiO_{1.3}$ and μSi deliver almost the same ICE of 94% (**Figure 3**A,B). This ICE improvement compared with the full cell using pristine anodes (44% for $SiO_{1.3}$ and 79% for μSi) is expected due to the delicate control of the prelithiation process. More importantly, the capacity retention of the full cell improves to 77% from 55% after 200 cycles by using prelithiated $SiO_{1.3}$ with 0.7% CE increase for every cycle on average (Figure 3C,E). A comprehensive comparison between the full cell performance achieved in this study and prior results can be found in Table S2 (Supporting Information). Our investigation not only shows a remarkable ICE of 94%, but also establishes the highest level of cycling stability. The same improvement trend is observed for the full cell using prelithiated μSi (Figure 3D,E), where the capacity retention increases from 24% to 44%. Despite the improvement, the full cell using prelithiated Si shows much lower capacity retention (44% *vs.* 77%) and average CE (99.5% *vs.* 99.9%) compared with that using prelithiated $SiO_{1.3}$. This obvious difference can be explained from both the bulk structure evolution and interface stability.

A key challenge for the application of Si is the volume expansion (≈300%) during its lithiation, which leads to the disruption of the SEI layer, continuous electrolyte consumption due to newly formed SEI, and electrode pulverization.[33,34] Cross section images were collected using scanning electron microscopy (FIB-SEM) to evaluate electrode thickness after the cycling in full cells, as shown in **Figure 4**. After 100 cycles, the prelithiated μSi anode thickness increases relatively by 28% compared with that after the initial cycle (12.4 μm *vs.* 9.7 μm). It should be noted this volume expansion is not trivial considering the thickness evaluation is performed at the delithiation state of the anode. In contrast, the thickness of the prelithiated $SiO_{1.3}$ anode only increases relatively by 3% after 100 cycles (Figure 4A,B). The much lower volume ex-

pansion of $SiO_{1.3}$ can be ascribed to both the bulk sub-oxide matrix and interface stabilization. Electrochemical impedance spectroscopy (EIS) of the full cell was then conducted to explore the interface impedance changes during extended cycles. Figure 4C,F show the Nyquist plots of the full cells prepared using the prelithiated anodes after the initial cycle and after 100 cycles, as well as the corresponding fitting plots using the equivalent circuit. R1, R2, and R3 represent electrolyte resistance, SEI resistance, and interface charge transfer resistance, respectively.[35] It turns out the interfacial resistance (R2 and R3) increases dramatically from 18 to 135 Ω after 100 cycles (Figure S7, Supporting Information) for the full cells using prelithiated μSi anodes. While a slight increase (29 Ω) is observed for the prelithiated $SiO_{1.3}$ anodes after 100 cycles. Since the LFP cathode side is relatively stable in the full cell, the EIS analysis well manifests the interface of prelithiated $SiO_{1.3}$ is more intact than the μSi over long-term cycling.

2.3. SEI Composition and Structure of Prelithiated Si-based Anodes

Further analysis of SEI composition and structure at the nanoscale is then performed to understand the prelithiation effect on the interface stabilization of $SiO_{1.3}$ anode. To compare the SEI formed in the electrochemical reaction, the pristine $SiO_{1.3}$ anode discharged in the half cell to the same potential as the prelithiated sample was also prepared. To prevent the washing effect on removing the fragile and/or reactive SEI components such as carbonate and oxides,[36] no solvent was introduced in all the samples preparation process for (S)TEM and energy dispersive X-ray (EDX) analysis. As shown in **Figure 5**A,B, the SEI formed through the prelithiation process shows a mosaic microstructure with uniform elemental distribution including C, F, Si, and P. It should be noted that the SEI species containing C, F, Si, and P can originate from both electrolyte decomposition and parasitic reactions occurring between $SiO_{1.3}$ and $LiPF_6$ during the prelithiation process. In contrast, a layered microstructure is observed for the SEI formed in the electrochemical process, where C, F, and P are in the outer layer of the SEI and the inner layer mainly consists of Si compounds. This obvious difference can be confirmed and quantified by the EDX line scan analysis, as shown in Figure S8 (Supporting Information). EDX Si line scan results in Figure S8 (Supporting Information) clearly indicate the formation of different microstructures of SEI through distinct lithiation processes. In the typical electrochemical process, slow C-rate is applied for the lithiation process so that different SEI components will form close to the equilibrium conditions. As predicted by the differential capacity curves in Figure 1C, the electrolyte decomposition byproducts, such as Li_2CO_3 and LiF, appear on the surface of particles first. And then lithium ions will pass through this outer layer to trigger the conversion of SiO_2 to lithium silicates and oxides to form the inner layer of SEI. While the short-circuit prelithiation process drives concentrated Li^+ flux together with strong electric field around the contact points, which results in the SEI formation far away from the thermodynamically stable state. All the SEI reactions occur almost simultaneously to construct the observed mosaic microstructure. The present hypothesis regarding the generation of distinct SEI microstructures during various lithiation processes is further supported by the
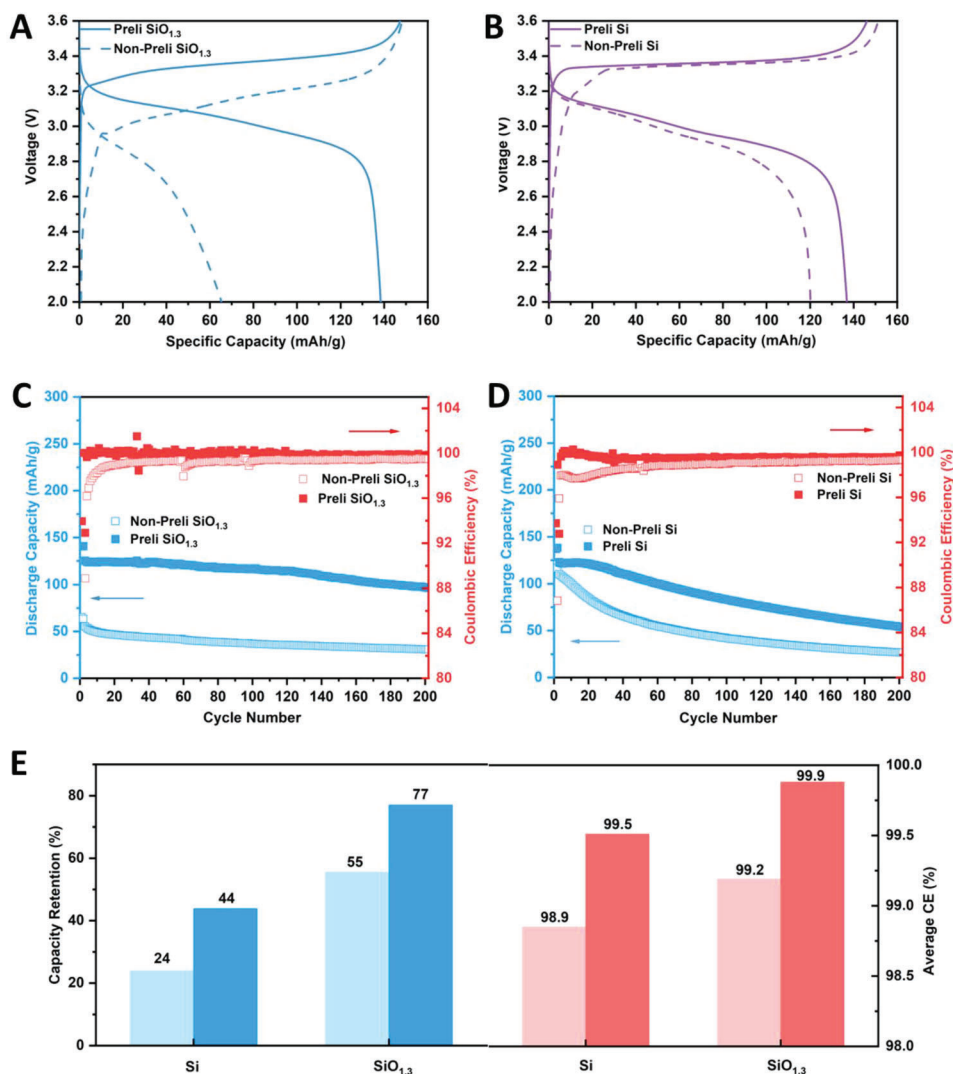
**ADVANCED
SCIENCE NEWS**

www.advancedsciencenews.com

**ADVANCED
ENERGY
MATERIALS**

www.advenergymat.de

Figure 3. A) Initial cycle voltage profile and C) long-term cycle performance of prelithiated and non-prelithiated $SiO_{1.3}$ in full cell with LFP cathode. Note the ICE of the full cell with non-prelithiated $SiO_{1.3}$ is not present in C) since the range has been adjusted to enhance the visibility of average CE variations during extended cycling. B) Initial cycle voltage profile and D) long-term cycle performance of prelithiated and non-prelithiated μSi in full cell with LFP cathode. E) Capacity retention and average CE comparison of prelithiated and non-prelithiated $SiO_{1.3}$ and μSi in full cell.

STEM-EDX analysis conducted on μSi anodes, as illustrated in Figure S9 (Supporting Information).

High resolution transmission electron microscopy (HRTEM) was then performed to detect the crystalline component of the SEI for both prelithiated $SiO_{1.3}$ and μSi. To protect thin surface layer from electron dose damage, all the HRTEM images in this work were recorded under cryogenic temperature, following our best sample transfer and imaging protocols.[37] The HRTEM image and the corresponding fast Fourier transform (FFT) pattern of the pristine and prelithiated $SiO_{1.3}$ electrodes are shown in **Figure 6**A,B. In the pristine state of $SiO_{1.3}$, the amorphous phase is found to be dominant with nanosized Si (as highlighted with the white area in the HRTEM image) based on the FFT spots of (111) plane of the diamond cubic structure. The pristine $SiO_{1.3}$ particle can thus be described as a mixture of nanosized Si and amorphous SiO_2, which is consistent with our XRD analysis.

After the prelithiation, the inset FFT pattern in Figure 6B illustrates the coexistence of LiF, Li_2CO_3, Li_2O, Li_4SiO_4, Li_2SiO_3, and Li-Si alloy species distributed in the interface area by matching the lattice spacings (Table S3, Supporting Information) of corresponding species with the pattern. All the identified prelithiation products correspond well with the differential capacity analysis for the three distinctive reactions. The uniform mixing of these products in the interface region supports the mosaic model proposed based on the EDX analysis. While the SEI formed in the typical electrochemical process with slow C-rate contains electrolyte decomposition byproducts (LiF, Li_2CO_3, etc.) as the outer layer and lithium silicate (Li_4SiO_4) as the inner layer, as shown in Figure S10 (Supporting Information). This observation is consistent with the layered microstructure of SEI under the equilibrium conditions. It is then as expected, the prelithiated μSi also illustrates the mosaic microstructure of SEI due
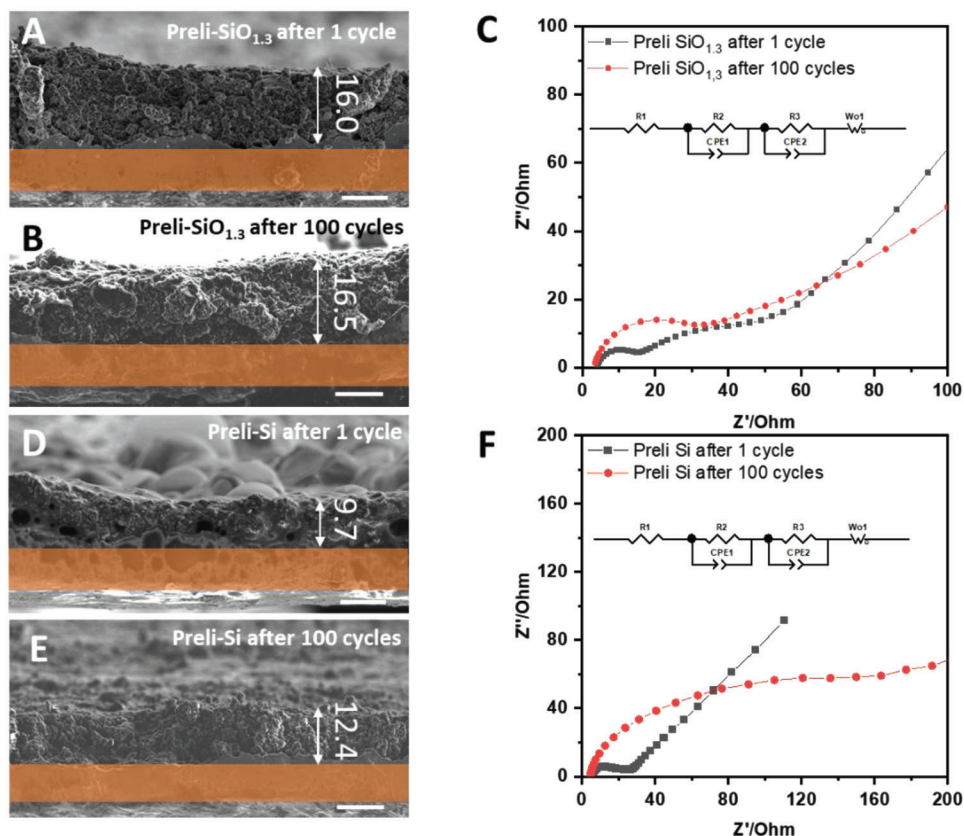
Figure 4. SEM cross section images of prelithiated $SiO_{1.3}$ after A) 1 cycle and B) 100 cycles and C) the impedance change of full cells upon cycling. SEM cross section images of prelithiated μSi after D) 1 cycle and E) 100 cycles and F) the impedance change of full cells upon cycling. All the scale bars in SEM images represent 10 μm. The orange bar in each SEM image indicates the location of the Cu current collector.
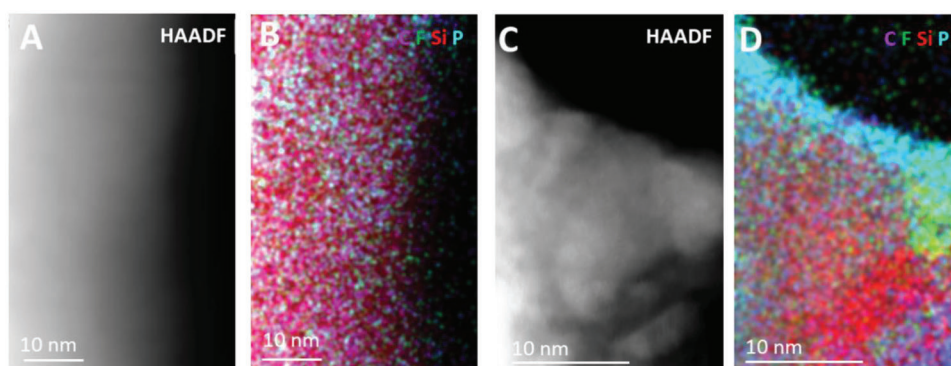

Figure 5. A) HAADF image of prelithiated $SiO_{1.3}$ using the short-circuit electrochemical method and B) its corresponding EDX mapping. C) HAADF image of lithiated $SiO_{1.3}$ in the half cell to the same potential as the prelithiated sample and D) its corresponding EDX mapping.

to the direct contact (Figure 6C,D). Compared with the prelithiated $SiO_{1.3}$, only Li_4SiO_4 is identified in the interface of prelithiated μSi. Note the lithium silicate in the prelithiated μSi is originated from the intrinsic thin oxide layer on the pristine sample (Figure 6C).

We then performed XPS depth profiling on the surface of the $SiO_{1.3}$ and μSi anode after the prelithiation to analyze the chemical composition of SEI layers. The results in two core levels of Si

2p and O 1s are shown in **Figure 7**. Both samples were profiled using high energy large Ar⁺ clusters (10 keV) so that the depth profile was completed with a sputter rate of 2 nm min⁻¹. The binding energy values of various Li_xSiO_y phases were determined in previous studies of Li_2SiO_3 and Li_4SiO_4.[38] It is important to note that a wider range of binding energy was used to fit Li_2SiO_3 and Li_4SiO_4 peaks as an approximation to interpret bonding distribution in the amorphous matrix. After the prelithiation, the Si

ADVANCED
SCIENCE NEWS

www.advancedsciencenews.com
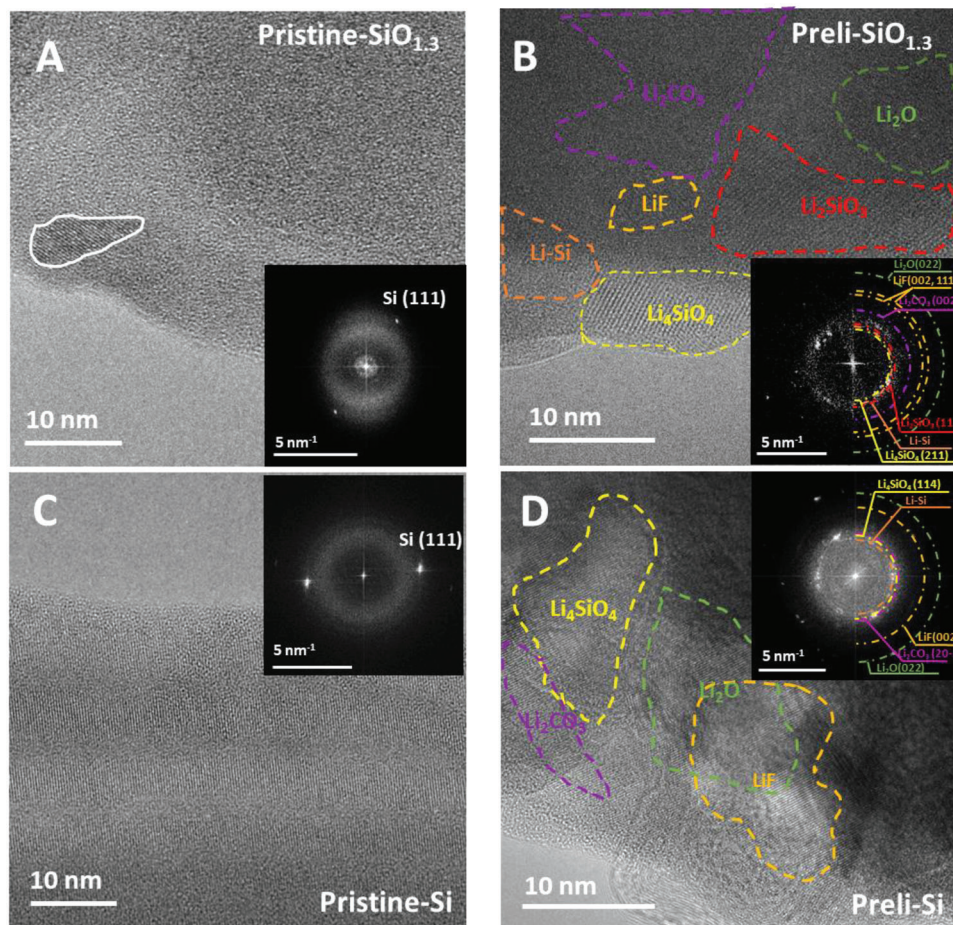
ADVANCED
ENERGY
MATERIALS

www.advenergymat.de

Figure 6. HRTEM images of pristine A) and prelithiated B) SiO$_{1.3}$ with corresponding FFT patterns. HRTEM images of pristine C) and prelithiated D) μSi with corresponding FFT patterns.

2p spectra in Figure 7 show that the interface of SiO$_{1.3}$ is primarily composed of lithium silicates (101.3 eV for Li$_4$SiO$_4$ and 102.8 eV for Li$_2$SiO$_3$). The formation mechanism of these two lithium silicates have been well studied by solid state NMR in the previous work:[31]

$$4SiO \xrightarrow{Li^+,e^-} Li_4SiO_4 + Li_xSi \tag{1}$$

$$Li_4SiO_4 + 3Li_xSi \xrightarrow{Li^+,e^-} (1-y)Li_4SiO_4 + yLi_2SiO_3 + 3SiO_{y/3} \tag{2}$$

Where the SiO$_2$ component is lithiated to form Li$_4$SiO$_4$ in the first step, and the molar ratio between the Li$_4$SiO$_4$ and Li$_2$SiO$_3$ depends on the depth of lithiation in the second step.

A much higher Li-Si alloy peak is observed in the prelithiated μSi, indicating the formation of a less conformal SEI layer. Only one type of lithium silicate (Li$_4$SiO$_4$) is identified in the SEI of prelithiated μSi, which is consistent with the HRTEM results. For O 1s spectra, the peaks at 532.0 and 529.0 eV are assigned to Li-Si-O and Li$_2$O species, respectively.[39] A larger amount of Li$_2$O can be found in the prelithiated SiO$_{1.3}$ than μSi due to the higher oxygen content in the structure. Other common components of SEI (LiF, P-F-O, Li$_2$CO$_3$) can also be iden-

tified in F 1s and C 1s spectra, as shown in Figure S11 (Supporting Information). No obvious difference of these electrolyte decomposition byproducts is found in the SEI of prelithiated SiO$_{1.3}$ and μSi.

2.4. Discussion on Mechanism of Cycling Performance Improvement via Prelithiation

The above (S)TEM and EDX results reveal different SEI formation pathways for prelithiation process by direct contact compared with the conventional electrochemical process. After prelithiation, a mosaic type SEI containing lithium silicates is formed for both SiO$_{1.3}$ and μSi anodes. While the electrolyte decomposition byproducts (LiF, Li$_2$CO$_3$, etc.) are dominant species on the surface of the anode particles through the slow C-rate discharge to the same lithiation potential. The ideal SEI requires good electronic resistivity and ionic conductivity, which is critical for interface stabilization over long-term cycling. Therefore, the electronic and ionic conductivity of several identified lithium silicates and electrolyte decomposition byproducts were measured, and the results are shown in **Table 1**. Lithium silicates exhibit at least two orders of magnitude
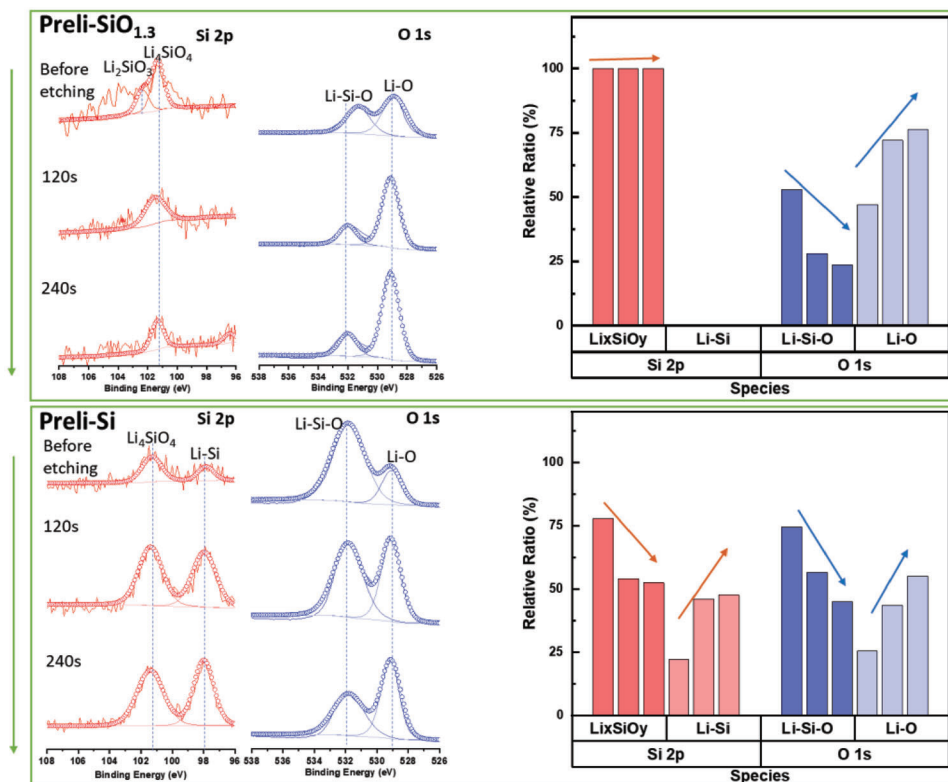
**ADVANCED
SCIENCE NEWS**

www.advancedsciencenews.com

**ADVANCED
ENERGY
MATERIALS**

www.advenergymat.de

Figure 7. The XPS depth profiling of Si 2p and O 1s spectra and quantitative analysis of different SEI components relative ratio for the prelithiated $SiO_{1.3}$ and μSi anodes.

Table 1. Major SEI components identified in prelithiated $SiO_{1.3}$ and μSi together with the measured physical properties of each component.

SEI components	Electronic conductivity [S cm^{-1}]	Ionic conductivity [S cm^{-1}]	Ionic-to-electronic conductivity ratio	Young's modulus [GPa]	$SiO_{1.3}$	Si
LiF	$\approx 10^{-12}$[40]	$\approx 10^{-8}$[40]	$\approx 10^4$	58.1–125[41]	√	√
Li_2CO_3	$\approx 10^{-10}$[42]	$\approx 10^{-9}$[43]	≈ 10	36.2–54.8[41]	√	√
Li_2O	$\approx 10^{-14}$[44]	$\approx 10^{-12}$[44]	$\approx 10^2$	163.58[45]	√	√
Li_4SiO_4	1.66×10^{-9}	8.57×10^{-7}	$\approx 10^3$	108.2–125.8[46]	√	√
Li_2SiO_3	1.72×10^{-9}	3.566×10^{-6}	$\approx 10^3$	110.7–126.7[46]	√	×
$Li_2Si_2O_5$	5.61×10^{-10}	2.778×10^{-7}	$\approx 10^3$	100.3[47]	√	×

better Li ion conductivity than that of LiF or Li_2CO_3. And the relatively high ionic-to-electronic conductivity ratio ($\approx 10^3$) of lithium silicates makes it sufficient to inhibit the unwanted electrochemical reactions. More importantly, compared with LiF and Li_2CO_3, the much higher mechanical strength of lithium silicates enables robust surface layer to sustain drastic volume fluctuation. The favorable combination of excellent conductivity and mechanical properties exhibited by lithium silicates contributes to improved cycling stability of both prelithiated anodes.

Compared with the prelithiated μSi, higher ratio of lithium silicates and lithium oxide exist in the SEI of the prelithiated $SiO_{1.3}$, which further improves the interface stability. As demonstrated in Figure S12 (Supporting Information), the mosaic SEI microstructure and silicates enriched composition well maintain

even after 180 cycles. The appearance of $Li_2Si_2O_5$ compound in the SEI after 180 cycles is consistent with the previous study on the structural evolution of SiO_x thin-film electrodes with subsequent lithiation/delithiation cycles.[29] Additionally, no bulk particle cracking is observed for the prelithiated $SiO_{1.3}$ after 100 cycles (Figure S13, Supporting Information). As summarized in the following schematics (**Figure 8**), the mosaic microstructure enabled by prelithiation is well maintained after long cycling in $SiO_{1.3}$. While for the μSi, the particle cracking is inevitable due to the large volume expansion ($\approx 300\%$) and limited amount of lithium silicates in SEI, which will result in the cycling failure eventually. Therefore, the preferred SEI microstructure and composition together with the lower volume expansion (< 150%) result in the superior cycling performance of prelithiated $SiO_{1.3}$ over μSi.

**ADVANCED
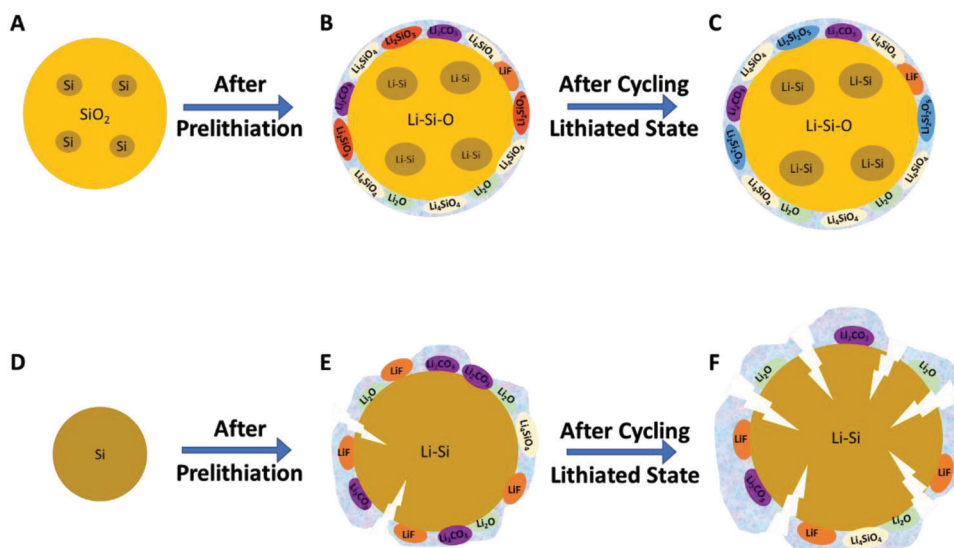SCIENCE NEWS**

www.advancedsciencenews.com

**ADVANCED
ENERGY
MATERIALS**

www.advenergymat.de

Figure 8. Schematics of prelithiation effect on cycling stability for both $SiO_{1.3}$ and μSi.

3. Conclusion

In summary, through a combined imaging, spectroscopy, and electrochemical analysis approach, this study reveals a mixed mosaic microstructure interface with better electrochemical and mechanical properties formed during the prelithiation process on the Si-based anodes using the direct contact method. This prelithiated interface is composed of lithium silicates, lithium oxide, and other typical electrolyte decomposition byproducts. All these components are uniformly mixed in the interface to form a mosaic microstructure. Due to the high ionic-to-electronic conductivity ratio and mechanical strength, lithium silicates enriched SEI is expected to enable long-term cycling stability. With more oxygen content to participate in the SEI formation process, the prelithiated $SiO_{1.3}$ anode based full cells with LFP cathode exhibit an initial specific discharge capacity of 138 mAh g^{-1} and an ICE of 94% at the current density of C/10. Moreover, 77% capacity retention is obtained after 200 cycles of charging and discharging at the current density of C/3. The ICE, specific capacity, and cycling stability of lithiated $SiO_{1.3}$-based full cells are improved significantly, indicating great prospects for the commercial application of Si-based anode materials.

4. Experimental Section

Sample Preparation: The pristine anode on a copper foil is composed of 70 wt. % silicon monoxide (99.9%, Alfa Aesar, active material) or micron silicon (1–5 µm, Alfa Aesar), 20 wt. % acetylene black (AB, Denka, conductive carbon), and 10 wt. % Poly (acrylic acid) (PAA, Mv 450000, Sigma–Aldrich, binder). The anode laminates were punched into 13 mm diameter discs with mass loading of ≈1.2 mg cm^{-2} for $SiO_{1.3}$ and ≈0.8 mg cm^{-2} for Si. The LiFePO$_4$ (LFP) cathode for the full cell was purchased from NEI (Areal capacity ≈1.25 mAh cm^{-2}, diameter 1/2 inch). 1 mol L^{-1} LiPF$_6$ was dissolved in ethylene carbonate (EC): dimethyl carbonate (DEC) (1:1, v/v) with 10% of fluoroethylene carbonate (FEC) (Gotion, USA) as the electrolyte.

Prelithiation Setup: Anode was wetted with 30 µL electrolyte and directly contact with Li metal chip (1 mm thick, 16 mm in diameter). 75 g weight was added to the top of the setup to ensure close contact between the $SiO_{1.3}$ electrode and Li metal chip during the prelithiation process with time monitor. Various prelithiated electrodes were assembled to the CR-2032-coin cell with Li metal as counter electrode and performed electrochemical testing. ICE ≈100% was considered as fully prelithiated anode condition.

Electrochemical Measurements: The fully-prelithiated anodes and LFP cathodes (N/P ratio 1.1–1.2) with 50 µL electrolyte were assembled in an Ar-filled glove box (H$_2$O < 0.1 ppm). The galvanostatic charge/discharge test was carried out at C/10-rate (1 C =170 mAh g^{-1}) for the initial two cycles in the voltage range of 2.0–3.6 V. The cells were then charged and discharged at C/3-rate for the rest of the cycles. All the tests were performed at room temperature. After cycling, the cells were dissembled in the Ar-filled glove box and the anode was rinsed with DMC solvent to remove salt residue on the surface. After drying at room temperature, the cycled anode materials were stored in the glove box for further characterization.

Conductivity Test: The sample powders were pressed into a 10 mm-diameter pellets at 625 MPa with the thickness measured. The EIS and DC polarization measurements were conducted at room temperature on Biologic using two titanium blocking electrodes enclosed by a polyetheretherketone holder. An applied AC potential of 30 mV over a frequency range from 1 to 1 MHz was used for the EIS measurement. A constant voltage of 0.1 V was applied for DC polarization. The stabilized current could be obtained when the ionic transportation was fully eliminated.

Scanning Electron Microscope: The experiment was carried out at 10 keV as the operating voltage at 0.1 nA with ETD detector under standard mode. Cross sections were prepared by cutting with scissors in the Ar-filled glovebox. The samples were cut carefully to prevent any mechanical damage. The samples were then transferred to the scanning electron microscope (SEM) chamber with the minimum exposure to air for the thickness analysis.

X-ray Diffraction: The X-ray diffraction (XRD) with Cu target was carried out using the capillary to eliminate the reaction from the air. The scanning region was 10–90° at 4-degree min^{-1}.

Transmission Electron Microscope: The samples were carefully scratched from the electrode and dispersed to the transmission electron microscope (TEM) grid (carbon side). A single-tilt liquid nitrogen cooling holder (Gatan 626) was used to cool the samples to ≈−170 °C to minimize electron beam damage where the TEM grids were sealed in heat-seal bags and transferred to TEM column using a purging home-made glovebox

2301041 (9 of 11)

filled with Ar gas. TEM images, and selected area electron diffraction (SAED) patterns were conducted on a JEOL JEM-2800F TEM, equipped with a Gatan Oneview camera operated at 200 kV. Pristine $SiO_{1.3}$ images were obtained on ThermoFisher Talos X200 equipped with a Gatan Oneview camera operated at 200 kV and UltraFast DualEELS Spectrum Imaging detector. The image was acquired with minimum beam damage at spot size 6 with a dose rate of 200 electrons/$Å^2$/s. The EELS spectrum and mapping were collected with an exposure time of 0.02 s, and the dispersion energy was 0.25 eV per channel.

X-ray Photoelectron Spectroscopy: X-ray photoelectron spectroscopy (XPS) was performed in an AXIS Supra XPS by Kratos Analytical. XPS spectra were collected using a monochromatized Al Ka radiation (hy = 1486.7 eV) under a base pressure of 10^{-9} Torr. To avoid moisture and air exposure, a nitrogen filled glovebox was directly connected to XPS spectrometer. Survey scans were performed with a step size of 1.0 eV, followed by a high-resolution scan with 0.1 eV resolution, for Li 1s, C 1s, O 1s, F 1s and Si 2p regions. All spectra were calibrated with adventitious carbon 1 s (284.6 eV) and analyzed by CasaXPS software. The etching condition used was Ar^+ mono mode, 10 keV voltage. The etching intervals were 120 s.

Supporting Information

Supporting Information is available from the Wiley Online Library or from the author.

Conflict of Interest

Y.S.M. was a technical advisor for Advano at the time of funding project.

Author Contributions

S.B., W.B., D.H.S.T. and Y.S.M. conceived the idea and designed the experiments. S.B. conducted electrochemical testing. K.Q. analyzed the EIS data. B.S. performed the XRD experiments. W.L. acquired the XPS data, and S.B. analyzed the data. S.B. acquired and analyzed the TEM data. W.B., D.H.S.T. and Y.S.M. supervised the research. S.B. wrote the manuscript. All authors contributed to the discussion and provided feedback on the manuscript.

Data Availability Statement

The data that support the findings of this study are available from the corresponding author upon reasonable request.

Keywords

cycling stability, interface stabilization, Li-ion batteries, prelithiation, Si-based anodes

[1] J. Liu, Z. Bao, Y. Cui, E. J. Dufek, J. B. Goodenough, P. Khalifah, Q. Li, B. Y. Liaw, P. Liu, A. Manthiram, Y. S. Meng, V. R. Subramanian, M. F. Toney, V. V. Viswanathan, M. S. Whittingham, J. Xiao, W. Xu, J. Yang, X. Q. Yang, J. G. Zhang, *Nat. Energy* **2019**, *4*, 180.

[2] M. Zhang, D. A. Kitchaev, Z. Lebens-Higgins, J. Vinckeviciute, M. Zuba, P. J. Reeves, C. P. Grey, M. S. Whittingham, L. F. J. Piper, A. Van der Ven, Y. S. Meng, *Nat. Rev. Mater.* **2022**, *7*, 522.

[3] X. Zuo, J. Zhu, P. Müller-Buschbaum, Y. J. Cheng, *Nano Energy* **2017**, *31*, 113.

[4] Z. Liu, Q. Yu, Y. Zhao, R. He, M. Xu, S. Feng, S. Li, L. Zhou, L. Mai, *Chem. Soc. Rev.* **2019**, *48*, 285.

[5] W. Bao, C. Fang, D. Cheng, Y. Zhang, B. Lu, D. H. S. Tan, R. Shimizu, B. Sreenarayanan, S. Bai, W. Li, M. Zhang, Y. S. Meng, *Cell Rep* **2021**, *2*, 100597.

[6] Y. Zhang, N. Du, D. Yang, *Nanoscale* **2019**, *11*, 19086.

[7] H. Chen, Y. Yang, D. T. Boyle, Y. K. Jeong, R. Xu, L. S. de Vasconcelos, Z. Huang, H. Wang, H. Wang, W. Huang, H. Li, J. Wang, H. Gu, R. Matsumoto, K. Motohashi, Y. Nakayama, K. Zhao, Y. Cui, *Nat. Energy* **2021**, *6*, 790.

[8] Z. Cao, X. Zheng, Q. Qu, Y. Huang, H. Zheng, Z. Cao, Q. Qu, H. Zheng, X. Zheng, Y. Huang, *Adv. Mater.* **2021**, *33*, 2103178.

[9] J. Chen, X. Fan, Q. Li, H. Yang, M. R. Khoshi, Y. Xu, S. Hwang, L. Chen, X. Ji, C. Yang, H. He, C. Wang, E. Garfunkel, D. Su, O. Borodin, C. Wang, *Nat. Energy* **2020**, *5*, 386.

[10] L. Jin, C. Shen, Q. Wu, A. Shellikeri, J. Zheng, C. Zhang, J. P. Zheng, L. Jin, J. Zheng, C. Zhang, C. Shen, Q. Wu, A. Shellikeri, J. P. Zheng, *Adv. Sci.* **2021**, *8*, 2005031.

[11] Y. Zhang, B. Wu, G. Mu, C. Ma, D. Mu, F. Wu, *J Energy Chem* **2022**, *64*, 615.

[12] J. Wang, H. Wang, J. Xie, A. Yang, A. Pei, C. L. Wu, F. Shi, Y. Liu, D. Lin, Y. Gong, Y. Cui, *Energy Storage Mater.* **2018**, *14*, 345.

[13] Y. Li, Y. Qian, J. Zhou, N. Lin, Y. Qian, *Nano Res.* **2022**, *15*, 230.

[14] V. L. Chevrier, L. Liu, R. Wohl, A. Chandrasoma, J. A. Vega, K. W. Eberman, P. Stegmaier, E. Figgemeier, *J. Electrochem. Soc.* **2018**, *165*, A1129.

[15] G. M. Overhoff, R. Nölle, V. Siozios, M. Winter, T. Placke, *Batter Supercaps* **2021**, *4*, 1163.

[16] H. J. Kim, S. Choi, S. J. Lee, M. W. Seo, J. G. Lee, E. Deniz, Y. J. Lee, E. K. Kim, J. W. Choi, *Nano Lett.* **2016**, *16*, 282.

[17] Q. Meng, G. Li, J. Yue, Q. Xu, Y. X. Yin, Y. G. Guo, *ACS Appl. Mater. Interfaces* **2019**, *11*, 32062.

[18] J. Fu, H. Liu, L. Liao, P. Fan, Z. Wang, Y. Wu, Z. Zhang, Y. Hai, G. Lv, L. Mei, H. Hao, J. Xing, J. Dong, *Front Chem* **2018**, *6*, 624.

[19] M. Y. Yan, M. Y. Yan, G. Li, G. Li, J. Zhang, Y. F. Tian, Y. F. Tian, Y. X. Yin, Y. X. Yin, C. J. Zhang, K. C. Jiang, Q. Xu, H. L. Li, Y. G. Guo, *ACS Appl. Mater. Interfaces* **2020**, *12*, 27202.

[20] B. Huang, T. Huang, L. Wan, A. Yu, *ACS Sustainable Chem. Eng.* **2021**, *9*, 648.

[21] Q. Sun, J. Li, C. Hao, L. Ci, *ACS Appl. Mater. Interfaces* **2022**, *14*, 14284.

[22] D. J. Chung, D. Youn, S. Kim, D. Ma, J. Lee, W. J. Jeong, E. Park, J. S. Kim, C. Moon, J. Y. Lee, H. Sun, H. Kim, *Nano Energy* **2021**, *89*, 106378.

[23] M. Gautam, G. K. Mishra, A. Ahuja, S. Sau, M. Furquan, S. Mitra, *ACS Appl. Mater. Interfaces* **2022**, *14*, 17208.

[24] K. H. Kim, J. Shon, H. Jeong, H. Park, S. J. Lim, J. S. Heo, *J. Power Sources* **2020**, *459*, 228066.

[25] Y. Zhu, W. Hu, J. Zhou, W. Cai, Y. Lu, J. Liang, X. Li, S. Zhu, Q. Fu, Y. Qian, *ACS Appl. Mater. Interfaces* **2019**, *11*, 18305.

**ADVANCED
SCIENCE NEWS**

www.advancedsciencenews.com

**ADVANCED
ENERGY
MATERIALS**

www.advenergymat.de

[26] H. Wang, M. Zhang, Q. Jia, D. Du, F. Liu, M. Bai, W. Zhao, Z. Wang, T. Liu, X. Tang, S. Li, Y. Ma, *Nano Energy* **2022**, *95*, 107026.

[27] C. Shen, R. Fu, Y. Xia, Z. Liu, *RSC Adv.* **2018**, *8*, 14473.

[28] K. Schulmeister, W. Mader, *J Non Cryst. Solids* **2003**, *320*, 143.

[29] J. H. Cho, X. Xiao, M. W. Verbrugge, B. W. Sheldon, *ACS Appl. Energy Mater.* **2022**, *5*, 13293.

[30] F. Aureli, M. Ciprotti, M. D'amato, E. D. N. da Silva, S. Nisi, D. Passeri, A. Sorbo, A. Raggi, M. Rossi, F. Cubadda, *Nanomaterials* **2020**, *10*, 888.

[31] K. Kitada, O. Pecher, P. C. M. M. Magusin, M. F. Groh, R. S. Weatherup, C. P. Grey, *J. Am. Chem. Soc.* **2019**, *141*, 7014.

[32] J. I. Lee, N. S. Choi, S. Park, *Energy Environ. Sci.* **2012**, *5*, 7878.

[33] H. Tian, H. Tian, W. Yang, F. Zhang, W. Yang, Q. Zhang, Y. Wang, J. Liu, S. R. P. Silva, H. Liu, G. Wang, *Adv. Funct. Mater.* **2021**, *31*, 2101796.

[34] K. Schroder, J. Alvarado, T. A. Yersak, J. Li, N. Dudney, L. J. Webb, Y. S. Meng, K. J. Stevenson, *Chem. Mater.* **2015**, *27*, 5531.

[35] M. Zhang, H. Liu, Z. Liu, C. Fang, Y. S. Meng, *ACS Appl. Energy Mater.* **2018**, *1*, 3369.

[36] H. S. Hirsh, B. Sayahpour, A. Shen, W. Li, B. Lu, E. Zhao, M. Zhang, Y. S. Meng, *Energy Storage Mater.* **2021**, *42*, 78.

[37] J. Alvarado, M. A. Schroeder, M. Zhang, O. Borodin, E. Gobrogge, M. Olguin, M. S. Ding, M. Gobet, S. Greenbaum, Y. S. Meng, K. Xu, *Mater. Today* **2018**, *21*, 341.

[38] B. Philippe, R. Dedryvère, J. Allouche, F. Lindgren, M. Gorgoi, H. Rensmo, D. Gonbeau, K. Edström, *Chem. Mater.* **2012**, *24*, 1107.

[39] Y. Li, W. Li, R. Shimizu, D. Cheng, H. Nguyen, J. Paulsen, S. Kumakura, M. Zhang, Y. S. Meng, Y. Li, W. Li, R. Shimizu, M. Zhang, Y. S. Meng, D. Cheng, H. Nguyen, J. Paulsen, S. Kumakura, *Adv. Energy Mater.* **2022**, *12*, 2103033.

[40] T. G. Stoebe, *J. Phys. Chem. Solids* **1967**, *28*, 1375.

[41] H. Shin, J. Park, S. Han, A. M. Sastry, W. Lu, *J. Power Sources* **2015**, *277*, 169.

[42] H. Ghobarkar, O. Schäf, *Cryst. Res. Technol.* **1993**, *28*, 855.

[43] H. Huo, J. Luo, V. Thangadurai, X. Guo, C. W. Nan, X. Sun, *ACS Energy Lett.* **2020**, *5*, 252.

[44] S. Lorger, R. Usiskin, J. Maier, *J. Electrochem. Soc.* **2019**, *166*, A2215.

[45] S. Hull, T. W. D. Farley, W. Hayes, M. T. Hutchings, *J. Nucl. Mater.* **1988**, *160*, 125.

[46] T. Tang, *J. At. Mol. Sci.* **2010**, *1*, 185.

[47] B. G. Simba, M. V. Ribeiro, P. A. Suzuki, M. F. R. P. Alves, K. Strecker, C. dos Santos, *J. Mech. Behav. Biomed. Mater.* **2019**, *98*, 179.

2301041 (11 of 11)